Effect of Ta Addition on Glass-Forming Ability and Structures of $Fe_{40}Co_{40}Zr_7V_2B_{11}$ Alloy

Y.M. Sun* and P.L. Zhang

College of Continuing Education, Jilin Normal University, 1301 Haifeng street, 136000 Siping, China

Received: 17.05.2023 & Accepted: 12.09.2023

Doi: 10.12693/APhysPolA.144.209 *e-mail: sunyaming@jlnu.edu.cn

$Fe_{40}Co_{40}Zr_7V_2B_{11-x}Ta_x$ ($x = 0, 1, 2$) alloy ribbons are prepared through single-roller melt spinning followed by annealing in a temperature range of 300–700°C. The influence of substituting Ta for V on the free and wheel surface structures of the samples is investigated. The addition of Ta improves the glass-formation ability owing to the large atomic radius of Ta atoms. The as-quenched $Fe_{40}Co_{40}Zr_7V_2B_{11}$ alloy is not amorphous, and α-Fe crystals are textured (200) on the free surface. Moreover, the as-quenched $Fe_{40}Co_{40}Zr_7V_2B_{10}Ta_1$ alloy is not completely amorphous, and a small amount of α-Fe crystals remains textured (200) on the free surface. The crystallization of the free surfaces of the $Fe_{40}Co_{40}Zr_7V_2B_{11}$ and $Fe_{40}Co_{40}Zr_7V_2B_{10}Ta_1$ alloys differs from those of the wheel-contacted surfaces. Both the free and wheel-contacted surfaces of the as-quenched $Fe_{40}Co_{40}Zr_7V_2B_9Ta_2$ alloy exhibit fully amorphous structures. The crystallization of the free surface of the $Fe_{40}Co_{40}Zr_7V_2B_9Ta_2$ alloy is similar to that of the wheel-contacted surface. The ductility of the $Fe_{40}Co_{40}Zr_7V_2B_9Ta_2$ alloy is greater than that of the $Fe_{40}Co_{40}Zr_7V_2B_{11}$ and $Fe_{40}Co_{40}Zr_7V_2B_{10}Ta_1$ alloys. The addition of Ta significantly improves the glass-forming ability and ductility of the alloy.

topics: alloy, crystallization, cross-section, ductility

1. Introduction

FeCo-based amorphous nanocrystalline soft magnetic alloy is one of the important research directions of Fe-based soft magnetic alloys, which has the advantages of amorphous alloy and all kinds of traditional soft magnetic materials, having aroused great interest from scholars [1–7]. It plays a great role in promoting the progress of modern electric power and electrical industry technology. This kind of alloy material presents excellent energy-saving and environmental protection characteristics during the processes of sample preparation and product use. Fe-based amorphous alloy products are mainly amorphous strips, which are used in transformer cores and other electrical applications. A study on the plasticity and brittleness of Fe-based alloy strips is necessary to permit their widespread use [8].

Different alloying elements were added to the alloys to improve the structure and properties of Fe-based alloys. The effect of adding alloying elements or partially substituting different elements has been previously reported in reviews [9, 10]. Only a few studies have been reported on the effect of Ta addition on Fe-based soft magnetic alloys [11–13]. Furthermore, there is little research on the glass-forming ability and ductility.

TABLE I

Enthalpy of mixing between B/Ta and other elements.

	Enthalpy of mixing [kJ/mol] for			
	Fe	Co	Zr	V
B	−26	−24	−71	−42
Ta	−15	−24	+3	−7

Nanocrystalline soft magnetic materials are typically two-phase systems comprising ferromagnetic nanocrystals embedded in a ferromagnetic amorphous matrix. The amorphous-crystallization method is one of the most commonly used methods for preparing FeCo-based nanocrystalline magnetic alloy materials, such as the amorphous alloy precursor, and in the crystallization of amorphous alloys. In industry and the laboratory, the single roll rapid quenching method is often used to prepare the amorphous alloy precursor, which is used to form alloy ribbons. The formation of nanocrystalline materials prepared from rapidly quenched amorphous alloys via thermal treatment strongly depends on the structure of the original amorphous state and the local atomic ordering. For the alloy ribbon prepared

by single roll rapid quenching method, the cooling rate decreased as going from the wheel surface to the free surface of the ribbon [14]. The gradient of the cooling rate across the thickness of the ribbon during melt-spinning causes a variation in the surface morphology and microstructure between the free side and wheel side of the as-spun ribbon [15]. Moreover, during the melting spinning process of Fe-based amorphous alloys with high Fe contents, it is easy for α-Fe crystals to precipitate in the free surface, particularly at a low wheel rotating speed.

In this study, $Fe_{40}Co_{40}Zr_7V_2B_{11-x}Ta_x$ (x = 0, 1, 2) alloys were selected as research objects. The structures of three kinds of alloys between the free surface and the wheel-contacted surface were elucidated.

2. Experimental part

Ingots of $Fe_{40}Co_{40}Zr_7V_2B_{11-x}Ta_x$ (x = 0, 1, 2) alloys with nominal compositions (the composition is given in atomic percent) were prepared by arc melting and then remelted 4 times through magnetic stirring. Alloy ribbons were prepared from the ingots by a single-roller melt spinning with a copper-wheel rate of 38 m/s, and then the ribbons were annealed at crystallization peak temperatures for 40 min at 300, 500, 550, 600, 650, and 700°C.

The structures of the samples were investigated by X-ray diffraction (XRD, D/max 2500 PC, Cu K_α, λ = 1.5406 Å) and scanning electron microscope (SEM, S-570).

3. Results and discussion

The XRD patterns of the as-quenched $Fe_{40}Co_{40}Zr_7V_2B_{11}$, $Fe_{40}Co_{40}Zr_7V_2B_{10}Ta_1$, and $Fe_{40}Co_{40}Zr_7V_2B_9Ta_2$ alloys are shown in Fig. 1 for both the free surface (a) and the wheel-contacted (b) surfaces. A distinct diffraction peak corresponding to the (200) crystal plane of α-Fe is evident for the free surface of the as-quenched $Fe_{40}Co_{40}Zr_7V_2B_{11}$ alloy. This indicates the absence of an amorphous structure and the presence of textured (200) α-Fe(Co) crystals on the free surface. When adding 1 at.% Ta, the intensity of the crystallization diffraction peak is significantly reduced, whereas a minor amount of the α-Fe(Co) crystals remains textured (200) on the free surface. The free surface of the as-quenched $Fe_{40}Co_{40}Zr_7V_2B_9Ta_2$ alloy exhibit a fully amorphous structure, whereas the wheel-contacted surfaces of all three as-quenched alloys exhibits amorphous structures, characterized only by a halo peak. The inclusion of Ta in the melt-spun alloy effectively mitigates the pronounced (200) plane peak of α-Fe(Co) crystals, significantly decreasing the peak intensity. Clearly, the glass-forming ability increases with the addition of Ta.

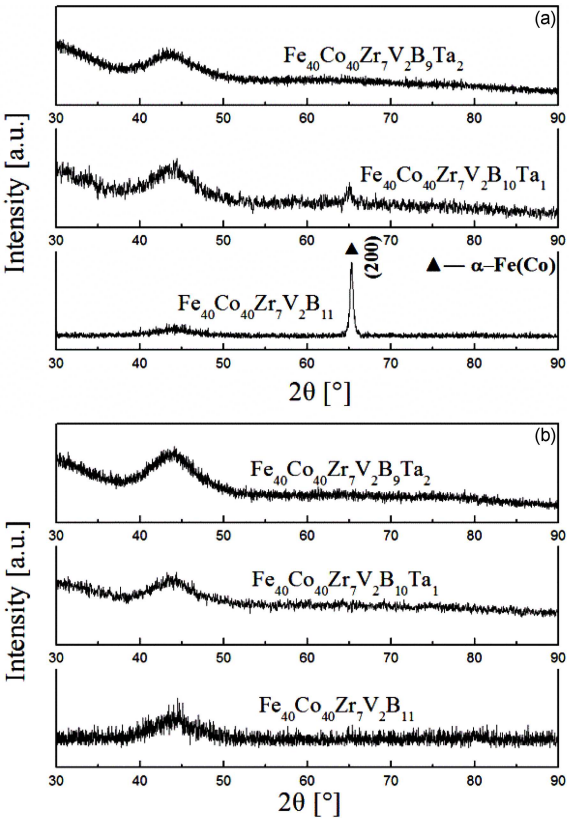

Fig. 1. XRD patterns of as-quenched $Fe_{40}Co_{40}Zr_7V_2B_{11}$, $Fe_{40}Co_{40}Zr_7V_2B_{10}Ta_1$, and $Fe_{40}Co_{40}Zr_7V_2B_9Ta_2$ alloys; (a) free surface, (b) wheel-contacted surface.

Differences between the free surface and the wheel-contacted surfaces are evident in the $Fe_{40}Co_{40}Zr_7V_2B_{11}$ alloy. The free surface reveals a diffraction peak related to the (200) crystal plane, whereas no such peak is observed on the wheel-contacted surface. For the $Fe_{40}Co_{40}Zr_7V_2B_{10}Ta_1$ alloy, a small amount of textured (200) α-Fe(Co) crystals remain on the free surface; hence, no completely amorphous structure is formed. Conversely, both the free and wheel-contacted surfaces of the as-quenched $Fe_{40}Co_{40}Zr_7V_2B_9Ta_2$ alloy exhibit fully amorphous structures. During single-roller melt-spinning, the wheel-contacted surface directly contacts the copper roll, with the cooling rate decreasing when going from the wheel surface to the free surface of the ribbon, thus inducing a difference in structure between both surfaces.

Table I shows the mixing enthalpies of B/Ta with other elements [16], where Ta exhibits small negative enthalpies compared to B. Substituting B with Ta could reduce the mixing enthalpy of the alloy and its glass-forming ability, which is in contrast to the result in Fig. 1.

Apart from the mixing enthalpy, the glass-forming ability is also related to the atomic radius of the atom. The atomic radii of Fe, Co, Zr, V, B, and

Ta atoms are 0.124, 0.125, 0.160, 0.132, 0.082, and 0.143 nm, respectively [17]. The greater the atomic size difference between alloy elements, the better the improvement in the liquid-phase atomic bulk density for obtaining amorphous alloys [18]. The increase in Ta, along with its large atomic radius, enhances the mismatch of atomic sizes and improves the glass-forming ability.

When the $Fe_{40}Co_{40}Zr_7V_2B_{11}$ alloy was folded, the alloy fractured easily. When the $Fe_{40}Co_{40}Zr_7V_2B_{10}Ta_1$ alloy was folded twice, the alloy fractured. When the $Fe_{40}Co_{40}Zr_7V_2B_9Ta_2$ alloy was folded repeatedly, the alloy fractured. The addition of Ta increases the ductility. Figure 2 shows the SEM images of the cross-sections of three types of alloys after fracture. The cross-section can be divided into three areas, namely, the free surface (b, f, j), the central (c, j, k), and the wheel-contacted surface (d, h, l) areas.

For the $Fe_{40}Co_{40}Zr_7V_2B_{11}$ alloy, numerous fine particles appear on the surface. The intermediate transition area is relatively flat. The wheel-contacted surface exhibits some vein patterns. For the $Fe_{40}Co_{40}Zr_7V_2B_{10}Ta_1$ alloy, the appearance close to the free surface is relatively flat. From the free surface to the wheel-contacted surface, several dimpled areas can be observed in the central area. The wheel-contacted surface presents vein patterns. The vein pattern appears when the glass is adiabatically heated during the operation of a shear band[†1]. The vein patterns reflect the local viscous flow of amorphous metals [19] and result from a rapid drop in the material viscosity. For the $Fe_{40}Co_{40}Zr_7V_2B_9Ta_2$ alloy, the free surface presents a dense network-like structure, which disappears from the free surface to the wheel-contacted surface, presenting numerous vein patterns. These deep vein patterns are greater than those in the $Fe_{40}Co_{40}Zr_7V_2B_{10}Ta_1$ alloy.

The XRD patterns from the free and wheel-contacted surfaces of the as-quenched $Fe_{40}Co_{40}Zr_7V_2B_{11}$ (a), $Fe_{40}Co_{40}Zr_7V_2B_{10}Ta_1$ (b), and $Fe_{40}Co_{40}Zr_7V_2B_9Ta_2$ (c) alloys after annealing at different temperatures are shown in Fig. 3. The three types of alloys exhibited different crystallization properties; this is attributed to the differences in the rapidly quenched structures.

The crystallization of the free (Fig. 3a) and wheel-contacted (Fig. 3b) surfaces of $Fe_{40}Co_{40}Zr_7V_2B_{11}$ differ significantly. When the annealing temperature is 300°C, the structure is similar to that of the rapidly quenched state. After annealing at 500°C, the (110) diffraction peak of the α-Fe(Co) phase is also observed in addition to the (200) diffraction peak. With increasing annealing temperature, the intensities

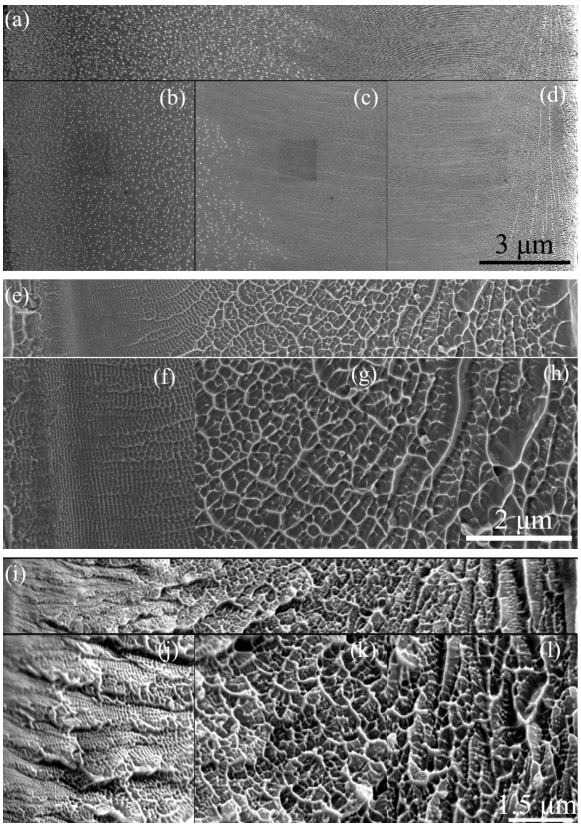

Fig. 2. SEM images of cross-sections of as-quenched $Fe_{40}Co_{40}Zr_7V_2B_{11}$ (a–d), $Fe_{40}Co_{40}Zr_7V_2B_{10}Ta_1$ (e–h), and $Fe_{40}Co_{40}Zr_7V_2B_9Ta_2$ (i–l) alloys: (a, e, i) panorama, (b, f, j) free surface area, (c, j, k) central area, (d, h, l) wheel-contacted surface area.

of the diffraction peaks increase. At an annealing temperature of 700°C, the $ZrCo_3B_2$ and BCo_3 phases are observed alongside the α-Fe(Co) phase. Throughout the crystallization process, the intensity of the (200) diffraction peak surpasses that of the (110) diffraction peak. No diffraction peak is observable on the wheel surface of the alloy at an annealing temperature of 300°C (Fig. 3b). Beyond 500°C, the (110), (200), and (211) diffraction peaks of the α-Fe(Co) phase become evident, although the intensities of the (200) and (211) diffraction peaks are weak. As the annealing temperature increases further, the intensities of the diffraction peaks increase.

For the $Fe_{40}Co_{40}Zr_7V_2B_{10}Ta_1$ alloy, at an annealing temperature of 300°C, the (200) diffraction peak of the α-Fe(Co) phase remains detectable on the free surface of the as-quenched alloy adjacent to the amorphous phase (Fig. 3c). This phenomenon resembles that of the rapidly quenched state. After annealing at 500°C, the (110) diffraction peak of the α-Fe(Co) phase is also observed next to the (200) diffraction peak. As the annealing temperature rises further, the intensity of the diffraction peak increases. Furthermore, the (200)

[†1]The shear bands contribute to the brittleness of metallic glasses.

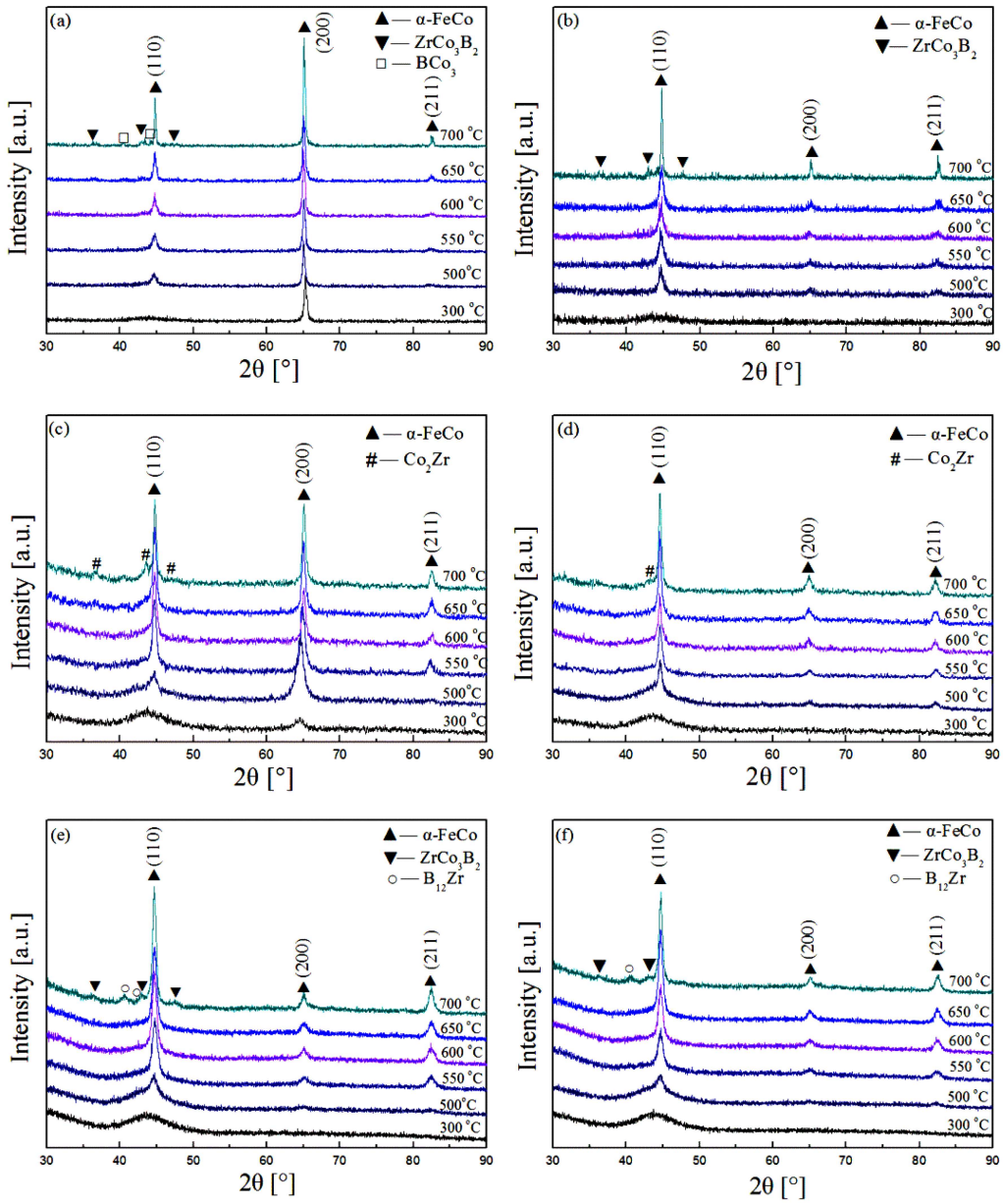

Fig. 3. XRD patterns of (a) $Fe_{40}Co_{40}Zr_7V_2B_{11}$, (b) $Fe_{40}Co_{40}Zr_7V_2B_{10}Ta_1$, and (c) $Fe_{40}Co_{40}Zr_7V_2B_9Ta_2$ alloys annealed at different temperatures; (a, c, e) free surface, (b, d, f) wheel-contacted surface.

diffraction peak of the α-Fe phase shifts to a higher angle, indicating the gradual dissolution of more Co atoms into α-Fe during crystallization. The intensity of the (200) diffraction peak is slightly higher than that of the (110) diffraction peak. At an annealing temperature of 700°C, the Co_2Zr phase is observed alongside the α-Fe(Co) phase. No diffraction peak is observable for the wheel surface of the alloy annealed at 300°C (Fig. 3d). Beyond 500°C, the (110), (200), and (211) diffraction peaks of the α-Fe(Co) phase become evident, with the intensities of (200) and (211) diffraction peaks being weak. With a further increase in annealing temperatures, the diffraction peak intensity increases. The crystallizations of free and wheel-contacted surfaces exhibit differences.

For the $Fe_{40}Co_{40}Zr_7V_2B_9Ta_2$ alloy, the crystallization of the free surface (Fig. 3e) is similar to that of the wheel-contacted surface of the alloy (Fig. 3f). No diffraction peak can be observed for the wheel surface of the alloy at 300°C. Above 500°C, the (110), (200), and (211) diffraction peaks of the α-Fe(Co) phase are observed, and the intensities of (200) and (211) diffraction peaks are weak. With a further increase in annealing temperatures, the diffraction peak intensity increases.

The addition of Ta affects the crystallization of the alloys. The crystallization of $Fe_{40}Co_{40}Zr_7V_2B_{11}$ on the free and wheel-contacted surfaces differs significantly. However, with increasing Ta content, the difference between the free surface and the wheel-contacted surface becomes smaller. The

crystallization of the free and wheel-contacted surfaces of the $Fe_{40}Co_{40}Zr_7V_2B_9Ta_2$ alloy is similar.

4. Conclusions

1. The as-quenched $Fe_{40}Co_{40}Zr_7V_2B_{11}$ and $Fe_{40}Co_{40}Zr_7V_2B_{10}Ta_1$ alloys do not form a complete amorphous structure, and α-Fe crystals are textured (200) on the free surface. Both the free and wheel-contacted surfaces of the as-quenched $Fe_{40}Co_{40}Zr_7V_2B_9Ta_2$ alloy exhibit an amorphous structure.
2. The addition of Ta affects the crystallization of the alloys. The crystallization of $Fe_{40}Co_{40}Zr_7V_2B_{11}$ differ markedly between the free and wheel-contacted surfaces. With increasing Ta content, the difference between the free and wheel-contacted surfaces decreases. The crystallization of the free and wheel-contacted surfaces is similar in the $Fe_{40}Co_{40}Zr_7V_2B_9Ta_2$ alloy.
3. Adding Ta can significantly improve the glass-forming ability and plasticity, and Ta is an effective additive element in component design.

Acknowledgments

This work was supported by the Sinoma Institute of Materials Research (Guang Zhou) Co., Ltd. and the Natural Science Foundation of Jilin Province (YDZJ202201ZYTS319). We would like to thank Editage (www.editage.cn) for English language editing.

References

[1] X.S. Li, Z.Y. Xue, X.B. Hou, G.Q. Wang, X. Huang, H.B. Ke, B.A. Sun, W.H. Wang, *Intermetallics* **131**, 107087 (2021).

[2] T. Liu, F. Kong, L. Xie, A. Wang, C. Chang, X. Wang, C. Liu, *J. Magn. Magn. Mater.* **441**, 174 (2017).

[3] Z. Hua, T. Feng, Y. Wu, W. Yu, Y. Liu, *Acta Phys. Pol. A* **141**, 630 (2022).

[4] Y. Gu, Y. H. Zhang, X. Li, J. Wang, B. Wang, K.M. Wang, *Phys. Met. Metallorg.* **121**, 123 (2020).

[5] F. Wang, A. Inoue, Y. Han, S.L. Zhu, F.L. Kong, E. Zanaeva, G.D. Liu, E. Shalaan, F. Al-Marzouki, A.Obaidf, *J. Alloys Compd.* **723** 376 (2017).

[6] L. Xue, W. Yang, H. Liu, H. Men, A. Wang, C. Chang, B. Long, *J. Magn. Magn. Mater.* **419**, 198 (2016).

[7] B. Zuo, X. Yu, X.N. Wang, Z.Q. Wang, *Met. Sci. Heat Treat.* **61**, 23 (2019).

[8] C. Wang, Z. Zhuang, F. Ding, Z. Lai, Q. Ye, J. Wang, *Mater. Today Commun.* **35**, 105637 (2023).

[9] H.R. Lashgari, D. Chu, S.S. Xie, H.D. Sun, M. Ferry, S. Li, *J. Non-Cryst. Solids* **391**, 61 (2014).

[10] T. Gheiratmand, H.R.M. Hosseini, *J. Magn. Magn. Mater.* **408**, 177 (2016).

[11] A. Puszkarz, M. Wasiak, A. Różański, P. Sovak, M. Moneta, *J. Alloy. Compd.* **491**, 495 (2010).

[12] I.V. Sterkhova, L.V. Kamaeva, V.I. Lad'yanov, N.M. Chtchelkatchev, *J. Mol. Liquids* **323**, 114636 (2021).

[13] A. Gupta, S.N. Kane, N. Bhagat, T. Kulik, *J. Magn. Magn. Mater.* **254**, 492 (2003).

[14] S. Niyomsoan, P. Gargarella, N. Chomsaeng, P. Termsuksawad, U. Kühn, J. Eckert, *Mater. Res.* **18**, 120 (2015).

[15] H.Y. Zhang, Y.P. Feng, Y.Y. Cheng, M. Dolors Bar, A. Altube, E. García-Lecina, F. Alcaide, E. Pellicer, T. Zhang, J. Sort, *ACS Omega* **2**, 653 (2017).

[16] A. Takeuchi, A. Inoue, *Mater. Trans.* **46**, 2817 (2005).

[17] O.N. Senkov, D.B. Miracle, *Mater. Res. Bull.* **36**, 2183 (2001).

[18] S.J. Poon, G.J. Shiflet, F.Q. Guo, V. Ponnambalam, *J. Non-Cryst. Solids* **317**, 1 (2003).

[19] C. Dun, H. Liu, L. Hou, L. Xue, L. Dou, W. Yang, Y. Zhao, B. Shen, *Appl. Phys. Lett.* **92**, 251906 (2008).